Polymorphism Influences Singlet Fission Rates in Tetracene Thin Films

Dylan H. Arias,[†,§] Joseph L. Ryerson,[†,§] Jasper D. Cook,[§] Niels H. Damrauer,[§] Justin C. Johnson[†]

[†]National Renewable Energy Laboratory, Golden, Colorado, 80401, United States
[§]Department of Chemistry and Biochemistry, University of Colorado, Boulder, Colorado, 80301, United States

S1. Theoretical calculation details

In both polymorphs'.cif files, one Tc molecule, labeled A in Fig. S1, sits at [*½ 0*] in the *ab*-plane. Molecule B sits at [*0 ½*], molecule C sits at [*1 ½*], and molecule D sits at [*1½ 0*]. Thus, to describe dimer AB in Fig. S1, we consider a translation vector [*a b*] = [*-½ ½*]. In other words, from the perspective of A in Fig. S1, molecule B sits half a unit cell backwards in the *a* direction and half a unit cell forwards in the *b* direction. By the same logic, the dimer AC can be described with [*a b*] = [*½ ½*] and the dimer AD with [*a b*] = [*1 0*]. The dimers in opposite directions, i.e. AB' ([*½ -½*]), AC' ([*-½ -½*]), and AD' ([*-1 0*]), are equivalent to AB, AC, and AD, respectively.

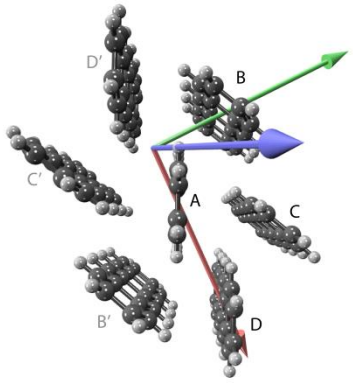

Figure S1. Representation of Tc cluster (http://iqmol.org) comparable to that shown in Fig. 1(d) for explanation of dimer designations in terms of translation vectors [*a b*]. The lattice directions are *a* (red), *b* (green), and *c* (blue; out of page). The central Tc molecule labeled A sits at [*a b*] = [*½ 0*] in the unit cell of the .cif files for both polymorphs.

We have applied a basic theory,[1] exploiting one-electron matrix elements, in order to estimate the diabatic coupling between a singlet exciton state (S_1S_0 or S_0S_1) of these dimer pairs and the SF product state written as a singlet-coupled pair of triplets (^{1}TT). The efficacy of this theory relative to more complex treatments in the literature has been recently argued by one of our authors.[1] Within the applied theory, there are several important assumptions. (1) We ignore, as is common in the literature,[2-4] a direct pathway coupling the singlet exciton state with ^{1}TT. (2) We assume, as has been extensively argued for polyacene systems,[5-8] that charge

transfer states are higher in energy than the reactant and product states and participate via a super-exchange mechanism.[4] These charge-transfer states are referred to as either ^{1}AC or ^{1}CA depending on which of the chromophores in the dimer is cationic (C) versus anionic (A). In the coupling expressions shown below, the energy difference between the singlet excited state reactant and the charge transfer state is referred to as ΔE_{CT}. (3) We describe states using the common formality of a four-orbital basis[4, 7-16] that starts (as described below) with dimer delocalized orbitals HOMO-1, HOMO, LUMO, and LUMO+1 that become transformed to HOMO and LUMO on each of the chromophores of the dimer. Finally, (4) we use one-electron off-diagonal elements of a Fock matrix to describe the relevant orbital couplings. Here the assumption being made, that has been tested in the literature, is that two-electron Coulomb terms are small and can be neglected.[2, 4, 17]

Our application of theory[1] requires a Fock matrix providing one-electron orbital coupling terms t_{AB} in a basis of HOMO and LUMO on respective chromophores A and B of a dimer pair: $t_{AB} = \langle \varphi_A | \hat{F} | \varphi_B \rangle$. To obtain these, we start with the HOMO-1, HOMO, LUMO, and LUMO+1 subspace of canonical Kohn-Sham orbitals obtained using a standard DFT protocol within the Q-CHEM software package[18, 19] (ωB97X-D density functional[20]; 6-31G* basis set). A Boys localization[21-23] procedure is then applied leading to four degenerate orthonormal orbitals where two are localized to each respective chromophore of the dimer pair. Finally, a diagonalization procedure is applied that focuses on 2×2 subspaces resulting in a HOMO/LUMO pair for each chromophore of the dimer. The final Fock matrix contains all values of t_{AB} within this four-orbital basis.

Expressions used to evaluate the diabatic coupling between reactant and product states under the assumptions (1) – (4) discussed above, are shown below in Eqs. S1 and S2[1, 4]:

$$SF\ Coupling_{(S_1S_0 \rightarrow {}^1TT)} = \left| \langle {}^1TT | \widehat{H_{el}} | {}^1CA \rangle \langle {}^1CA | \widehat{H_{el}} | S_1S_0 \rangle + \langle {}^1TT | \widehat{H_{el}} | {}^1AC \rangle \langle {}^1AC | \widehat{H_{el}} | S_1S_0 \rangle \right| / \Delta E_{CT} \approx \left| \sqrt{3/2}\,(t_{LH}t_{LL} - t_{HL}t_{HH}) \right| / \Delta E_{CT} \quad \text{(S1)}$$

$$SF\ Coupling_{(S_0S_1 \rightarrow {}^1TT)} = \left|\langle {}^1TT|\widehat{H_{el}}|{}^1AC\rangle\langle {}^1AC|\widehat{H_{el}}|S_0S_1\rangle + \langle {}^1TT|\widehat{H_{el}}|{}^1CA\rangle\langle {}^1CA|\widehat{H_{el}}|S_0S_1\rangle\right| /\Delta E_{CT} \approx \left|\sqrt{3/2}\,(t_{HL}t_{LL} - t_{LH}t_{HH})\right| /\Delta E_{CT} \quad \text{(S2)}$$

Two expressions are needed for those dimers in a herringbone configuration because the two chromophores are not related by translation. Therefore, SF coupling depends on which of the chromophores (A or B) contains the singlet excitation at the outset; i.e., S_1S_0 versus S_0S_1. We evaluate both sets of couplings and pick the largest value for purposes of comparison. Within each of these expressions, a sum of terms is required for evaluation of coupling. These two terms, respectively, correspond to electron-transfer and hole-transfer mediated pathways for SF and the interference of these pathways (constructive or destructive) leads to the coupling value.

Results obtained for three dimer pairs for both polymorphs are shown in Table S1. Values for one-electron inter-chromophore orbital coupling matrix elements (including sign) are shown in the top section of rows. In the next two sections are compiled product terms relevant for evaluation of Eqs. S1 and S2. Finally, we report in the last row of the table diabatic coupling values for SF that are obtained from the application of either Eq. S1 or S2 (depending on which produces the larger magnitude value shown in bold) using ΔE_{CT} = 600 meV. This value is chosen based on electroabsorption literature where CT states are identified to be in the range of 2.7 – 3.1 eV,[24] thus suggesting ΔE_{CT} in a range of 400 – 800 meV above the singlet exciton state of 2.32 eV.[25] The quantity we use – ΔE_{CT} = 600 meV – represents the median case. For our purposes the exact value of ΔE_{CT} is unimportant as we are ultimately interested in relative coupling as a function of dimer direction and polymorph. However, we do use the same CT energy for Tc I and Tc II because we estimate the variation between polymorphs to be small. Using the distances in the Fig. 1 caption, we estimate the largest change in dimer-pair distance between Tc I and Tc II is 7%. Based on a simple Coulomb argument with point charges, the CT energy for Tc II might be more energetically stable by 7%. Thus, the coupling would be 7%

larger for Tc II if all other things stayed the same. Since coupling is squared in the rate constant expressions, Tc II would have a 14% larger rate constant compared to Tc I based on this argument. The effects we see experimentally are much greater than this. In addition, the variation in orbital coupling matrix elements is much greater than this, and so would dominate the differences between Tc I and Tc II in overall coupling.

Summing squares of coupling values (308 meV^2 for Tc I versus 113 meV^2 for Tc II), it is seen that by these predictions, SF should be ~ 3 times faster in polymorph I in contrast to our observations. Within these data it is seen that coupling is larger for both polymorphs in the [-½ ½] and [½ ½] directions where the herringbone arrangement is in place. Within each of these directions and for each polymorph, it can be seen that the electron-transfer pathway to SF destructively interferes with the hole-transfer pathway (common sign in the products of relevant one-electron matrix elements). In the case of Tc I in the [½ ½] direction, the large value of coupling is achieved because there is a significant asymmetry in the importance of the electron-transfer pathway (governed by $\sqrt{3/2}\ t_{HL}\ t_{LL}$) compared to the hole-transfer pathway (governed by $\sqrt{3/2}\ t_{LH}\ t_{HH}$). In the case of Tc II in this same [½ ½] direction, the electron-transfer pathway and the hole-transfer pathway switch in their relative importance. While coupling in each pathway remains significant in Tc II, destructive interference between both pathways leads to a lower overall value of coupling compared to Tc I. These types of effects are difficult to predict based on geometric considerations alone (see Fig. 1(c)), and highlight the importance of orbital shape, curvature, and phase.

Table S1. One-electron inter-chromophore orbital coupling matrix elements (in meV) and related product terms calculated with the Boys method for noncovalent Tc dimers taken from Tc I and Tc II crystal structures. SF coupling values calculated via application of Eq. S1 or S2. All dimers are in the *ab* plane and correspond to a [*a b*] translation vector. See text in Supporting Information for clarification of [*a b*].

	Tc I [-½ ½]	Tc II [-½ ½]	Tc I [½ ½]	Tc II [½ ½]	Tc I [*1 0*]	Tc II [*1 0*]
t_{HH}	-91	100	35	-85	2	54
t_{LL}	83	93	88	-63	17	44
t_{HL}	-74	88	-104	-94	1	-69

t_{LH}	107	112	-39	-60	-1	-69
Product terms (meV^2) relevant for application of Eq. S1:						
$\sqrt{3/2}\ t_{LH}\ t_{LL}$	10909	12823	-4163	4680	-28	-3698
$\sqrt{3/2}\ t_{HL}\ t_{HH}$	8213	10809	-4495	9796	3	-4562
$\sqrt{3/2}(t_{LH}\ t_{LL} - t_{HL}\ t_{HH})$	2697	2014	331	**-5116**[a]	**-31**[a]	**864**[a]
Product terms (meV^2) relevant for application of Eq. S2:						
$\sqrt{3/2}\ t_{HL}\ t_{LL}$	-7543	10056	-11218	7327	28	-3698
$\sqrt{3/2}\ t_{LH}\ t_{HH}$	-11879	13783	-1668	6257	-3	-4562
$\sqrt{3/2}\ (t_{HL}\ t_{LL} - t_{LH}\ t_{HH})$	**4336**[a]	**-3727**[a]	**-9550**[a]	1070	31	864
SF Coupling /meV[a]	7.2	6.2	16	8.5	0.05	1.4

[a]Bolded values used in the calculation of SF coupling where ΔE_{CT} = 600meV.

S2. Film Deposition

Tetracene thin films were deposited using a Radak source in an Angstrom Engineering Nexdep thermal evaporator coupled to a glove box. Tetracene was placed in an alumina crucible and evaporation was driven by resistively heating a tungsten filament. This enabled samples to be deposited and sealed under inert conditions, thus preventing exposure to oxygen and water vapor. Depending on the desired film type and crystallite size, deposition rate and substrate temperature were varied from 0.5 – 5.0 Å/s and 85 – 340K. Deposition rate and total thickness were monitored by a quartz crystal microbalance operating around 60 MHz. Depositions were performed under vacuum at pressures near 10^{-6} - 10^{-7} Torr, and the temperature of the crucible housed in the Radak source typically ranged from 185 – 210°C, depending on the desired deposition rate.

Prior to time resolved measurements, films were sealed with a matching glass cover slip by placing a Surlyn (60 μm thick) frame outlining the film to be analyzed between the two cover slips. In a glovebox under inert atmosphere, this sandwich configuration was placed on a hot plate at 95°C for approximately 15 seconds to melt the Surlyn and pressed to seal. This prevents film photobleaching and oxygen quenching of triplet excitons, essential to probing the true singlet fission dynamics.

S3. X-Ray Diffraction

XRD measurements were collected on a Rigaku DMax 2500 X-ray Diffractometer operating in θ/2θ mode using Cu-Kα radiation (0.154 nm). Data were acquired with a scan speed of 1 degree per minute, scanning from 5 to 25 degrees. An alignment procedure was performed on a blank substrate before each measurement session to ensure precise measurement of intensity (counts/s) as a function of diffraction angle. Additional XRD data was collected from a D2 Phaser X-Ray Diffraction Desktop system (Bruker) using Cu-Kα radiation. The substrate was rotated during acquisition, and diffraction patterns were detected with a LYNXEYE array detector at a resolution of 0.03° between 5° and 25°.

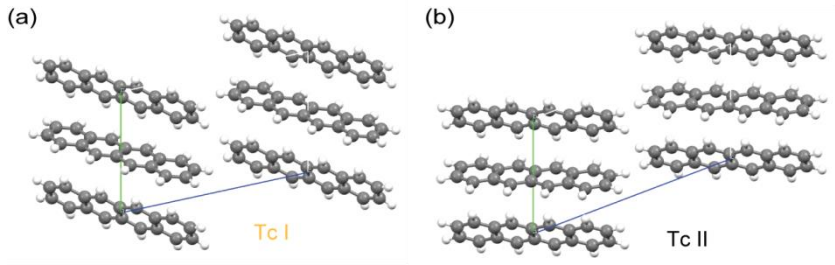

Figure S2. (a) Tc I crystal structure looking down the a-axis with the c-axis left to right. (b) Tc II crystal structure.

We used XRD to distinguish between Type I (Tc I) and Type II (Tc II) polymorphs. Tetracene molecules deposit with the long axis nearly perpendicular to the substrate plane, causing the *ab*-plane to be parallel to the surface and the c-axis to point towards the normal. Polycrystalline grains are isotropically distributed around the normal, leaving only the (00*c*) peaks observable in XRD. Tighter packing in the c-axis direction for Tc II compared to Tc I (Fig. S2a & b) leads to the lower angles for the (001), (002), and (003) peaks for Tc II. Fig. S3 also shows the XRD patterns calculated from the crystal structures. The Tc I crystal structure was determined experimentally, while Tc II was calculated after extrapolation from the Tc II single crystal under high pressure.[26]

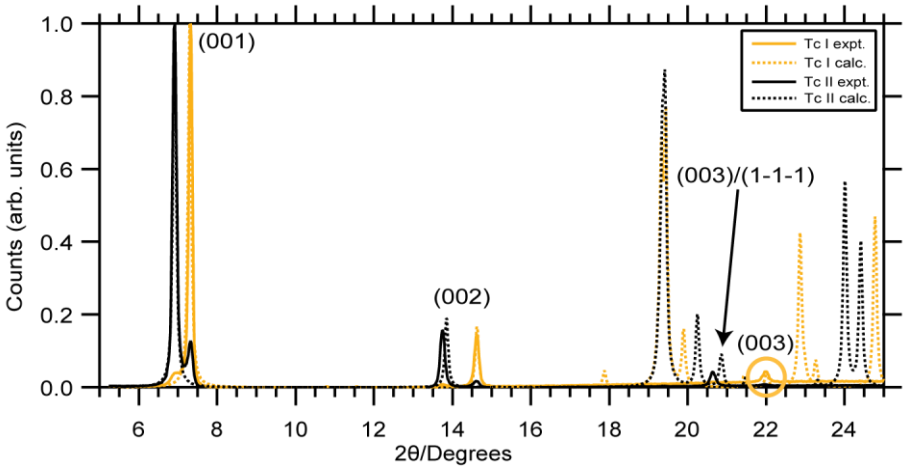

Figure S3. Comparison of experimental and calculated diffraction pattern for Tc I and Tc II. The (003) peak for Tc I is circled. The calculated (003) and (1-1-1) peaks for Tc II are strongly overlapped and merge into a single peak with a realistic linewidth of 0.1°-0.2°.

S4. Atomic Force Microscopy

AFM images and line scans for thickness determination were collected on a Park Systems AFM XE-70 using a scan speed of 0.2 – 0.5 Hz, adjusting gain depending on crystallite size and film thickness. Measurements were performed in tapping mode, scanning film areas of 100 μm^2 across 256 x 256 pixels resolution using a TAP-300G AFM tip. To determine film thicknesses, line scans were taken over 4-6 different areas lightly marked with a razor blade. The height differences between the bare substrate and thin film were measured and averaged to determine film thicknesses. The thicknesses determined via AFM were within ±10% of the thickness specified during deposition using the quartz crystal microbalance.

S5. UV-vis and steady-state PL

Integrating sphere (IS) absorption measurements were performed on a Varian Cary 6000i with an Integrating Sphere Attachment. Transmittance and reflectance data were collected at 600 nm/min and were corrected with baseline and zero scans. Absorption was calculated by Eq. S3:

$$A = -\log(R + T) \qquad (S3)$$

IS measurements help correct for reflections and scattering not accounted for in standard UV-Vis extinction measurements. Slow deposition rates yielded films with large crystallites and a

large scattering background, whereas faster deposition rates yielded smaller crystallites with reduced scattering.

Fluorescence measurements were collected on a Horiba Yvon FL-1039/40 Fluorolog controlled by the Fluoressence Software package. An iHR320 Horiba Jobin Yvon monochromator along with a Spex Instruments S.A. Group Horiba Jobin Yvon Spectrum One G35 CCD camera were used to collect steady state fluorescence data on samples in the front-face collection configuration. Typical excitation wavelengths ranged from 400 – 500 nm, collecting steady-state photoluminescence (PL) data ranging from 300 – 900 nm. Excitation and emission slit widths used were 2 – 4 nm, depending on PL intensity, film thickness, etc. PL spectra were collected by averaging 16 scans with an integration time of 0.1 s.

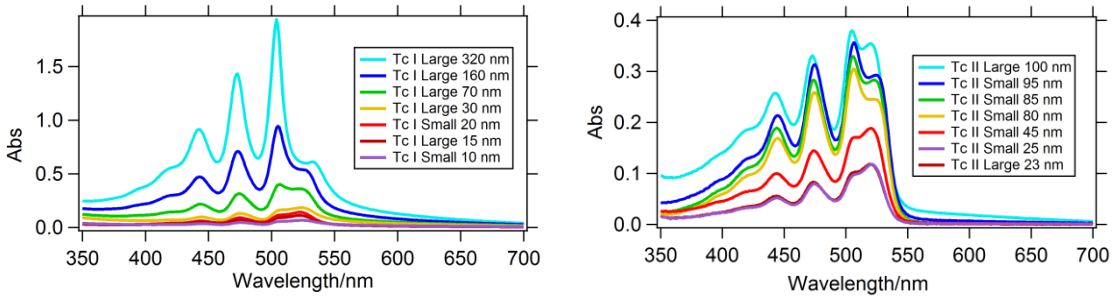

Figure S4. Thickness-dependent absorption for (a) Tc I and (b) Tc II. The amplitude of the Tc I 20 nm film is slightly unreliable because of non-uniform coverage of the substrate during deposition.

As observed previously in polycrystalline tetracene films,[27] thickness-dependent absorption intensity ratios of Davydov split peaks are evident for Tc I and Tc II films (Fig. S4). All the optical measurements used films with minimal saturation of the lowest energy Davydov peak (~80 nm thickness).

S6. Time-correlated single photon counting

Time-resolved fluorescence decays were obtained using a mode-locked femtosecond Ti:sapphire oscillator (Tsunami, Spectra Physics) operating at 790 nm and 82 MHz. The output was passed through a pulse picker (NEOS technologies) to achieve a repetition rate of 4.1 MHz, then frequency doubled using a *β*-barium borate (BBO) crystal to 395nm. The second harmonic

was filtered to remove residual fundamental before exciting the sample at 20° from normal. Emitted light was passed through a monochromator (Oriel 77250) before detection (Hamamatsu R3809U-50 microchannel plate detector) and analysis using a Becker-Hickl time-correlated single photon counting (TCSPC) card. The resulting data were fitted with a multiexponential decay function convoluted with an instrument response function (IRF) using a customized Igor procedure. The multiexponential decay expression is of the form presented in Eq. S4. Fig. S5 displays the entire TCSPC trace out to 80 ns, while the main text focuses on the singlet kinetics in the first few nanoseconds.

$$Fit = IRF \otimes \sum_{i=1}^{3} A_i e^{-\frac{t}{\tau_i}} \quad (S4)$$

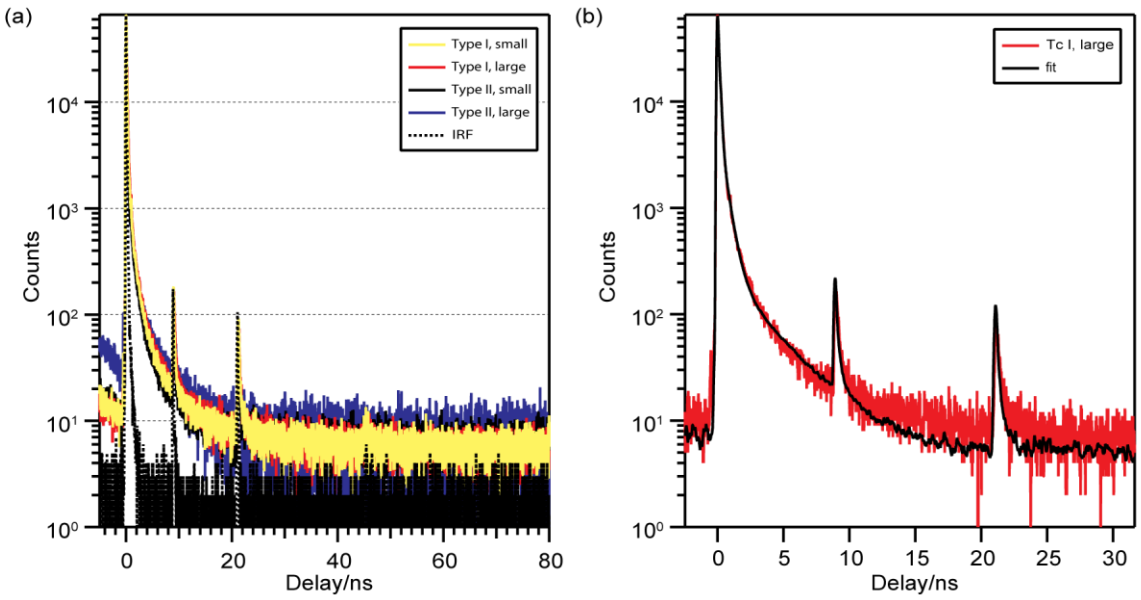

Figure S5. (a) TCSPC traces for the four films described in main text on a longer time scale. Peaks at ~10 ns and ~20 ns are due to incomplete rejection of oscillator pulses. (b) Tc I, large crystal TCSPC data overlaid with fit using Eq. 3 and parameters from Table S2 convoluted with the IRF.

Table S2. Fitted rate parameters for all four films. Amplitudes for exponentials (A_i) are listed as A_i/(A1+A2+A3).

	A_1	τ_1/ps	A_2	τ_2/ps	A_3	τ_3/ps
Tc I, large	0.958	82.7	0.040	471	0.002	3040
Tc I, small	0.977	66.9	0.022	563	0.001	3200
Tc II, small	0.981	49.4	0.018	442	0.001	2400

Tc II, large	0.987	39.2	0.012	482	0.001	3010

S7. Transient absorption

Ultrafast TA measurements were performed using a Coherent Libra Ti:sapphire laser system with an integrated Vitesse seed laser, Evolution pump laser, regenerative amplifier, and pulse stretcher and compressor. The Libra produces 4 W of sub-100 fs pulse duration, 800 nm pulses at 1 kHz, with a < 0.5% rms stability. A portion of this light is picked off and sent through a TOPAS-C collinear optical parametric amplifier with an energy conversion of about 30-35%, capable of generating a wide range of pump wavelengths, including the 400 nm pump used in this study. The remaining portion of the 800 nm light is passed through a delay stage and subsequently focused into a continuously moving CaF_2 crystal housed in an Ultrafast Systems LLC Helios Spectrometer. The Helios femtosecond transient absorption spectrometer generates a pump-probe delay using a delay stage capable of generating time delays out to about 5 ns, with an instrument time resolution of ~250 fs. The probe spectral range is about 350 - 800 nm. The Helios detectors are equipped with a dual 1024 pixel CMOS sensor for balancing, a spectral response of 350 - 950 nm, and an acquisition rate up to 2400 spectra / s.

The pump spot size was measured by focusing the pump through a series of pinholes with varying sizes and measuring the power before and after the pinhole. Transient spectra were collected as a function of pump fluence ranging from 10^{17} – 10^{19} excitations / cm^{-3} (a few nanojoules / pulse to a few hundred nanojoules / pulse). See Fig. S6 for a comparison of the two lowest fluence data, demonstrating the kinetics are fluence-independent.

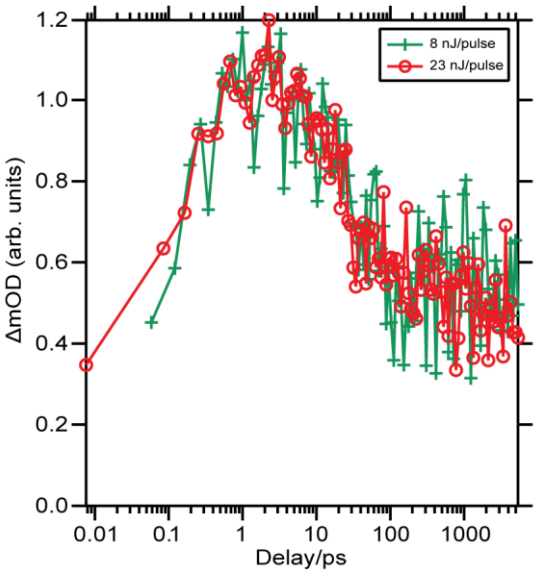

Figure S6. Single wavelength slices at 535 nm for Tc I, large crystallite films at two fluences, demonstrating fluence-independent kinetics.

Ultrafast Systems LLC Surface Explorer 4.0 Software Package was used for background and scatter subtraction, chirp correction, singular value decomposition (SVD), and global fitting of the principal components from SVD. At low fluences, SVD revealed two principal components, one decaying and the other rising, consistent with singlet and triplet states. The other components all represent experimental noise (Fig. S7a). At higher fluences, a ~1 ns oscillatory feature with a small singular value emerged, becoming clearer at the highest fluences (Fig. S7b); we associated this component with an acoustic mode caused by sample heating. Global fitting of the two principal components to a decaying exponential and an offset gave good fits of the kinetics (Fig. S7c). We associated the decay with a singlet-like component and the offset with a triplet-like component, although assigning the features directly is difficult because SVD requires no physical input, but is a purely mathematical procedure. Fig. S8 shows global fit decay constants for 80 nm and 40 nm thick films of Tc I and II, demonstrating the kinetics are not dependent on film thickness.

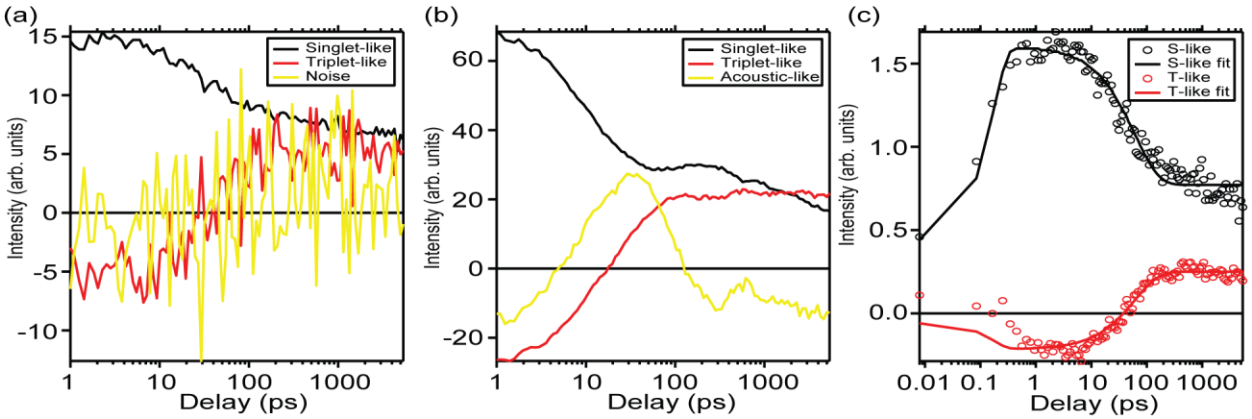

Figure S7. (a) Low fluence (1.83 x 10^{18} cm^{-3}) SVD. (b) High fluence (18.9 x 10^{18} cm^{-3}) SVD, with three components. (c) Global fit with a single exponential (61 ps) and offset (1.83 x 10^{18} cm^{-3}).

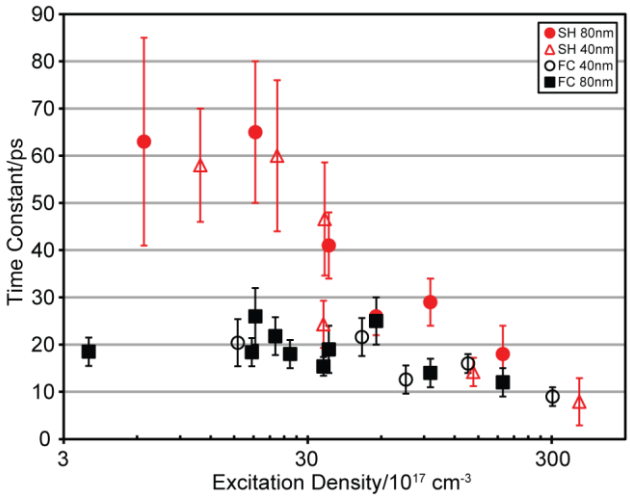

Figure S8. Global fit parameters for 80 nm and 40 nm thick films, demonstrating lack of thickness dependence.

Before further spectral and kinetic fitting was performed in Matlab, the oscillatory mode was subtracted from the data. An early time (~1 ps delay) and a late time (~5 ns delay) TA spectrum from the corrected dataset were assigned to represent singlet and triplet states, respectively. The entire TA dataset was fitted using the two characteristic spectra, with each spectrum for a particular delay fit to a linear combination of the two. From this spectral fitting, amplitudes of singlet and triplet components as a function of time were extracted. This procedure strictly extracts kinetic traces without an absolute magnitude. It is difficult to deconvolute excited state absorption, ground state bleach, and stimulated emission in tetracene because these features are broad and overlapping, making it difficult to apply a magnitude, i.e.

extinction coefficient, to the kinetic traces and to extract a triplet yield. The resulting kinetic curves were globally fitted to the model in Fig. 4 in the main text using the differential equations in Eq. S5:

$$\frac{d}{dt}\begin{pmatrix} S \\ T_p \\ T \\ G \end{pmatrix} = \begin{pmatrix} -\left(k_{sp}^{S} + k_{sf} + k_{SS}S\right) & k_{fus} & 0 & 0 \\ k_{sf} & -k_{sp}^{T} - k_{fus} - k_{diss} & k_{TT}T & 0 \\ 0 & 2k_{diss} & -k_{sp}^{T} - k_{TT}T & 0 \\ k_{sp}^{S} + k_{SS}S & k_{sp}^{T} & k_{sp}^{T} & 0 \end{pmatrix} \begin{pmatrix} S \\ T_p \\ T \\ G \end{pmatrix} \quad (S5)$$

We extracted rate constants for singlet and triplet decays, singlet fission, triplet fusion, triplet dissociation, and singlet exciton annihilation, similar to Wilson et al.[28] The singlet data was fit to the S state population, while the triplet data was fit to $T_{total} = 2T_p+T$ to account for all the contributing triplet population. The extracted kinetics and fits for all four films are shown in Fig. S9 and the rates are tabulated in Table S3. While the model allows for triplet-triplet annihilation, this rate was relatively unconstrained and tended towards the lower bound for the fit. Thus, we set this parameter to zero. The yield was calculated from a simulation using extremely low fluence (~10^{14} cm^{-3}) and evaluating T_{total} at ~1 ns.

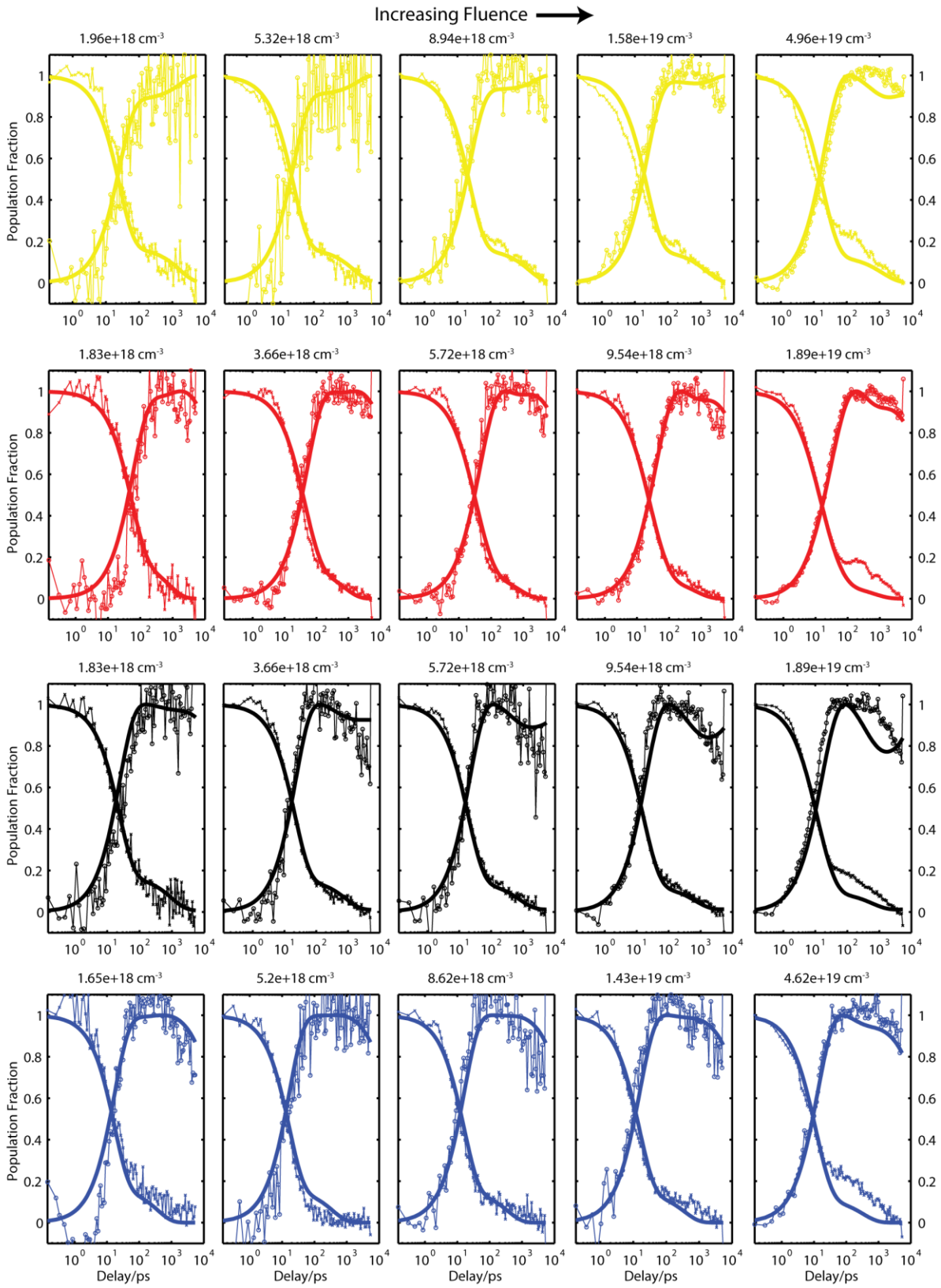

Figure S9. All extracted singlet and triplet dynamics and their fits. Excitation density (cm^{-3}) increases left to right. From top to bottom the films are: Tc I, small; Tc I, large; Tc II, small; Tc II, large.

Table S3. Extracted kinetic parameters for all four films. Fits are shown in Fig. S9.

	$1/k_{S,sp}$ [ps]	$1/k_{sf}$ [ps]	k_{SS} [10^{-21}cm^3/ps]	$1/k_{T,sp}$ [ps]	$1/k_{fus}$ [ps]	$1/k_{diss}$ [ps]	k_{TT} [cm^3/ps]	Triplet Yield [%]
Tc I, large	524	124	3.62	21,586	360	439	0	125
Tc I, small	12,500	35	0.56	1 µs	219	1,559	0	175
Tc II, small	500	36	3.86	31,814	99	268	0	155
Tc II, large	507	22	0.82	32,267	113	365	0	160

References

1. E. C. Alguire, J. E. Subotnik and N. H. Damrauer, *J. Phys. Chem. A*, 2014, **119**, 299-311.
2. M. B. Smith and J. Michl, *Annu. Rev. Phys. Chem.*, 2013, **64**, 361-386.
3. P. E. Teichen and J. D. Eaves, *J. Phys. Chem. B*, 2012, **116**, 11473-11481.
4. T. C. Berkelbach, M. S. Hybertsen and D. R. Reichman, *J. Chem. Phys.*, 2013, **138**, 114103.
5. S. R. Yost, J. Lee, M. W. B. Wilson, T. Wu, D. P. McMahon, R. R. Parkhurst, N. J. Thompson, D. N. Congreve, A. Rao, K. Johnson, M. Y. Sfeir, M. G. Bawendi, T. M. Swager, R. H. Friend, M. A. Baldo and T. Van Voorhis, *Nat. Chem.*, 2014, **6**, 492-497.
6. S. M. Parker, T. Seideman, M. A. Ratner and T. Shiozaki, *J. Phys. Chem. C*, 2014, **118**, 12700-12705.
7. T. Zeng, R. Hoffmann and N. Ananth, *J. Am. Chem. Soc.*, 2014, **136**, 5755-5764.
8. D. Casanova, *J. Chem. Theor. Comput.*, 2014, **10**, 324-334.
9. M. B. Smith and J. Michl, *Chem. Rev.*, 2010, **110**, 6891-6936.
10. E. C. Greyson, J. Vura-Weis, J. Michl and M. A. Ratner, *J. Phys. Chem. B*, 2010, **114**, 14168-14177.
11. T. C. Berkelbach, M. S. Hybertsen and D. R. Reichman, *J. Chem. Phys.*, 2013, **138**, 114102.
12. J. C. Johnson, A. Akdag, M. Zamadar, X. Chen, A. F. Schwerin, I. Paci, M. B. Smith, Z. Havlas, J. R. Miller, M. A. Ratner, A. J. Nozik and J. Michl, *J. Phys. Chem. B*, 2013, DOI: 10.1021/jp310979q.
13. D. Beljonne, H. Yamagata, J. L. Bredas, F. C. Spano and Y. Olivier, *Phys. Rev. Lett.*, 2013, **110**, 226402.
14. F. Mirjani, N. Renaud, N. Gorczak and F. C. Grozema, *J. Phys. Chem. C*, 2014, **118**, 14192-14199.
15. N. Renaud, P. A. Sherratt and M. A. Ratner, *J. Phys. Chem. Lett.*, 2013, **4**, 1065-1069.
16. L. Wang, Y. Olivier, O. Prezhdo and D. Beljonne, *J. Phys. Chem. Lett.*, 2014, **5**, 3345−3353.
17. Z. Havlas and J. Michl, Unpublished calculations.
18. Y. Shao, L. F. Molnar, Y. Jung, J. Kussmann, C. Ochsenfeld, S. T. Brown, A. T. B. Gilbert, L. V. Slipchenko, S. V. Levchenko, D. P. O'Neill, J. R. A. DiStasio, R. C. Lochan, T. Wang, G. J. O. Beran, N. A. Besley, J. M. Herbert, C. Yeh Lin, T. Van Voorhis, S. Hung Chien, A. Sodt, R. P. Steele, V. A. Rassolov, P. E. Maslen, P. P. Korambath, R. D. Adamson, B. Austin, J. Baker, E. F. C. Byrd, H. Dachsel, R. J. Doerksen, A. Dreuw, B. D. Dunietz, A. D. Dutoi, T. R. Furlani, S. R. Gwaltney, A. Heyden, S. Hirata, C.-P. Hsu, G. Kedziora, R. Z. Khalliulin, P. Klunzinger, A. M. Lee, M. S. Lee, W. Liang, I. Lotan, N. Nair, B. Peters, E. I. Proynov, P. A. Pieniazek, Y. Min Rhee, J. Ritchie, E. Rosta, C. David Sherrill, A. C. Simmonett, J. E. Subotnik, I. H. Lee Woodcock, W. Zhang, A. T. Bell, A. K. Chakraborty, D. M. Chipman, F. J. Keil, A. Warshel, W. J. Hehre, I. I. I. H. F. Schaefer, J. Kong, A. I. Krylov, P. M. W. Gill and M. Head-Gordon, *Phys. Chem. Chem. Phys.*, 2006, **8**, 3172-3191.
19. A. I. Krylov and P. M. W. Gill, *WIREs Comput. Mol. Sci.*, 2013, **3**, 317-326.

20. J. D. Chai and M. Head-Gordon, *Phys. Chem. Chem. Phys.*, 2008, **10**, 6615-6620.
21. S. F. Boys, *Rev. Mod. Phys.*, 1960, **32**, 296-299.
22. J. M. Foster and S. F. Boys, *Rev. Mod. Phys.*, 1960, **32**, 300-302.
23. C. Edmiston and K. Ruedenberg, *Rev. Mod. Phys.*, 1963, **35**, 457-465.
24. L. Sbastian, G. Weiser and H. Bassler, *Chem. Phys.*, 1981, **61**, 125-135.
25. J. J. Burdett, A. M. Muller, D. Gosztola and C. J. Bardeen, *J. Chem. Phys.*, 2010, **133**, 144506.
26. B. Schatschneider, S. Monaco, A. Tkatchenko and J. J. Liang, *J. Phys. Chem. A*, 2013, **117**, 8323-8331.
27. W. Hofberger, *Phys. Stat. Sol. (a)*, 1975, **30**, 271-278.
28. M. W. B. Wilson, A. Rao, K. Johnson, S. Gélinas, R. Di Pietro, J. Clark and R. H. Friend, *J. Am. Chem. Soc.*, 2013, **135**, 16680-16688.